Cell Reports
Physical Science

CellPress
OPEN ACCESS

Article

Electrochemical synthesis of high entropy hydroxides and oxides boosted by hydrogen evolution reaction

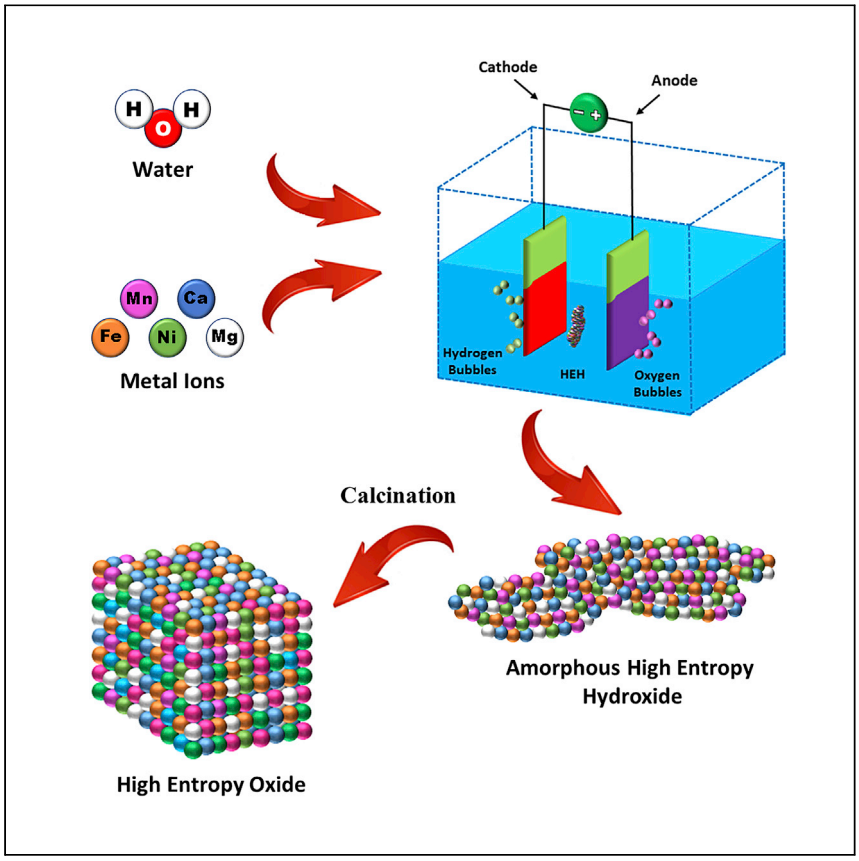

Ritter et al. report an electrochemical process for quick and scalable synthesis of high entropy hydroxide and oxide nanoparticles that avoids long synthesis times and high temperatures. The large variety of metal salt precursors allows for tuning of the composition for applications in catalysis, energy storage, and conversion.

Timothy G. Ritter, Abhijit H. Phakatkar, Md Golam Rasul, ..., Tolou Shokuhfar, Josué M. Gonçalves, Reza Shahbazian-Yassar

jmart437@uic.edu (J.M.G.)
rsyassar@uic.edu (R.S.-Y.)

Highlights

Aqueous electrochemical synthesis of high entropy hydroxides under ambient conditions

Green and substrate-free nanoparticle synthesis using inexpensive metal salts

Fast transformation from metal hydroxides to metal oxides with calcination process

Ability to scale to industrially promising applications

Ritter et al., Cell Reports Physical Science 3, 100847
April 20, 2022
https://doi.org/10.1016/j.xcrp.2022.100847

Cell Reports
Physical Science

CellPress
OPEN ACCESS

Article

Electrochemical synthesis of high entropy hydroxides and oxides boosted by hydrogen evolution reaction

Timothy G. Ritter,[1] Abhijit H. Phakatkar,[2] Md Golam Rasul,[3] Mahmoud Tamadoni Saray,[3] Lioudmila V. Sorokina,[1] Tolou Shokuhfar,[2] Josué M. Gonçalves,[3,*] and Reza Shahbazian-Yassar[3,4,*]

SUMMARY

Conventional synthesis techniques for high entropy materials often require prolonged processes or the use of complex fabrication steps. Here, we report on a scalable method to synthesize high entropy hydroxide and oxide nanoparticles using electrochemical synthesis in an aqueous environment. The current density parameter was set to create a non-equilibrium condition where the hydrogen evolution reaction results in a turbulent environment facilitating the formation of nanoparticles within the electrolyte. Using this approach, we demonstrate the synthesis of both binary (Fe, Mn) and quinary (Fe, Mn, Ni, Ca, Mg) metal hydroxide and oxide nanoparticles. The chemical and microscopy analysis shows that the high entropy nanoparticles can be synthesized as a hydroxide without any post processing and as an oxide through a calcination process with atomic scale mixing of all elements. The synthesis of high entropy nanoparticles is important for applications targeting catalysis, energy storage and conversion, filtration, and environmental engineering.

INTRODUCTION

High entropy materials generally consist of five or more elements incorporated together to form a single solid solution.[1] Their study has led to unique properties in magnetism, corrosion prevention, conductivity, water purification, catalysis, and energy storage.[2–9] One material subset of high entropy materials are high entropy hydroxides, which incorporate hydroxide into the crystal lattice.[10] There are several methods that have previously been used to synthesize high entropy hydroxide nanoparticles such as co-precipitation, pulsed laser, and cathodic reduction.[6,8,9,11–13] Co-precipitation methods require the delicate control of process parameters and require long amounts of time for synthesis.[6–8,13] Pulsed laser methods have faster synthesis times, but require the use of specialized equipment.[11] Cathodic reduction methods also requires long synthesis times to collect powder.[12]

In addition to the high entropy hydroxides, a second subset of high entropy materials are high entropy oxides, which are a variant of entropy stabilized materials that incorporate oxygen into the crystal lattice.[4] Several studies have shown unique properties associated with high entropy oxides such as large dielectric constants, high Li^+ conductivity ($>10^{-3}$ S cm^{-1}), and high cyclability (600 cycles) for use in reversible energy storage.[3,4,14] Several methods have been developed to produce high entropy oxide nanomaterials. Some of the more common techniques are mechanical alloying (e.g., ball milling), thermal based (e.g., carbothermal shock and

[1]Department of Civil & Materials Engineering, University of Illinois at Chicago, Chicago, IL 60607, USA

[2]Department of Biomedical Engineering, University of Illinois at Chicago, Chicago, IL 60607, USA

[3]Department of Mechanical & Industrial Engineering, University of Illinois at Chicago, Chicago, IL 60607, USA

[4]Lead contact

*Correspondence: jmart437@uic.edu (J.M.G.), rsyassar@uic.edu (R.S.-Y.)

https://doi.org/10.1016/j.xcrp.2022.100847

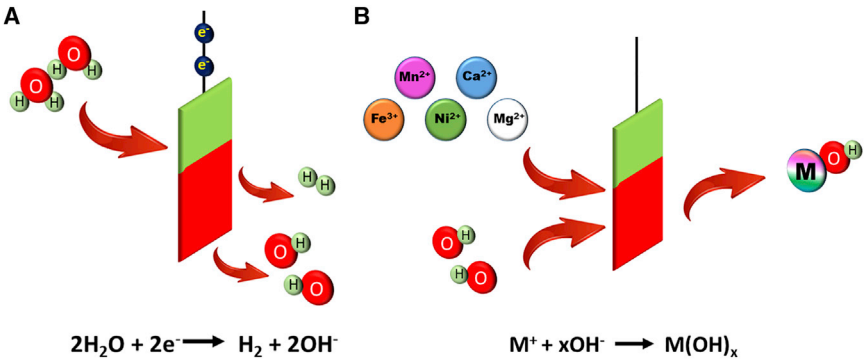

Figure 1. The proposed mechanism for the formation of HEH NPs under high current density ECS
(A) Hydrogen evolution reaction in aqueous electrolyte.
(B) Synthesis of HEH NPs by ECS.

flame spray pyrolysis), and wet chemistries (e.g., co-precipitation). Ball milling techniques typically require significant processing time to ensure chemical mixing of all the elements.[1,14,15] The flame spray pyrolysis technique uses a thermal shock through high temperature flame (approximately 1900°C) to produce high entropy oxide nanoparticles.[16] This process requires a robust setup with a high temperature flame and a method to generate aerosol precursor spray requiring specialized equipment, such as nebulizers or spray nozzles.[4,17] Wet chemical synthesis for high entropy oxide nanomaterials via co-precipitation route possesses the ability to produce high yields during synthesis. However, the process requires delicate control of chemical reaction parameters during multiple steps over extended periods of time during synthesis.[18]

The majority of electrochemical synthesis (ECS) applications focus on creating thin film systems using a variety of solvents such as water, dimethylformamide, and dimethyl sulfoxide.[19–23] Electrochemical thin film synthesis is capable of producing high-quality films for corrosion, catalysis, and energy storage applications, but the high entropy material is bound to the electrodes they are deposited on.[2,20,24,25] The use of organic solvents and bound material on the electrodes limits the scope of high entropy material applications for future large-scale production.

The present work demonstrates the ability of synthesizing substrate-free high entropy hydroxides and oxide nanoparticles by the selection of processing parameters, resulting in the breakdown of the aqueous electrolyte. This is done without the addition of additives to increase conductivity using an electrochemical synthesis technique and the hydrogen evolution reaction. The study includes the detailed microstructural and chemical oxidation state analysis of the high entropy hydroxides and oxides which can lead to future industrial scalability of these nanomaterials.

RESULTS

Electrochemical synthesis of amorphous high entropy hydroxides

The formation of the high entropy hydroxides (HEH) is the result of a two-step process. A schematic overview of the synthesis process is presented in Figure 1. In the first step, seen in Figure 1A, the hydrogen evolution reaction occurs. This process is the result of the breakdown of the aqueous electrolyte, and which causes water to break down to form hydrogen gas and hydroxide ions at the cathode ($2H_2O + 2e^- \rightarrow H_2 + 2OH^-$). Furthermore, the oxygen evolution reaction takes place simultaneously at the anode. In the second step, seen in Figure 1B, the hydroxide ions and the metal salt cations

combine to form the HEH nanoparticles ($M^+ + xOH^- \rightarrow M(OH)_x$). The equations for both reactions can be seen in Figure 1. After synthesis, the nanoparticles were collected from the electrolyte solution using centrifugation Figure S1 shows electrolyte solution before and after ECS. Figure S2 shows the voltage vs time for the ECS. Video S1 shows the slow motion synthesis of the HEH nanoparticles (NPs) during ECS.

In this study, a combination of the aqueous solvent and high current densities greatly decreases the times needed to produce HEH from hours to minutes without the need for specialized equipment. The high current densities make the ECS process capable of producing substrate-free nanoparticles with high yields. A direct result of the higher current densities is an increase in bubble formation around the electrodes caused by the breakdown of water into its gaseous components. For low current/voltage applications, a diffuse layer model, based on the Nerst-Planck equation, can be used to determine pH_s (near the surface pH) around the electrodes.[26] Bubble formation changes the model by taking into account different factors, such as convective flow, bubble distribution, bubble coalescence, and the fact that the layer surrounding the electrodes changes from a solid-solution interface to a two-phase gas-liquid system.[26] The bubble formation can also increase the transport of species across the diffuse layer.[26] A second effect of higher current densities is an increase in ion velocities.[27–29] The use of high current densities requires higher voltages creating a stronger electric field between the electrodes. The stronger electric field has the direct effect of increasing the ion velocities in solution as they move to the electrode, which increases the kinetics in the system.

The nanoparticles that form in the electrolyte can be easily separated from the suspension through centrifugation, where they can be cleaned and dried. Although HEH nanoparticles start to form shortly after the current is applied, within 20 min all the precursors in the solution is used. The production yield can be further increased and fine-tuned by tailoring the process parameters including the applied current, using electrodes with larger surface area, or by increasing the electrolyte concentration. These factors are known to play a role in other electrodeposition techniques.[30] With the addition of a calcination process, the HEH nanoparticles can be transformed into high entropy oxide (HEO) nanoparticles.

Morphology of HEHs under various current densities

To examine how synthesis conditions affects the HEH NPs, the synthesis was performed at various current densities (10, 116, and 232 mA/cm^2) and the morphology of the synthesized NPs was studied. It has been shown that electrochemical deposition processes below the breakdown threshold of the electrolyte can result in thin films of binary or multi-elemental compositions.[20–23,31–33] Thin films are more likely to form during low current and voltage conditions due to the lower kinetic energies that are available during synthesis. With lower currents and voltages, the electric field is reduced leading to slower ECS process kinetics.[30] Under the low current/voltage conditions, the NPs tend to deposit onto the electrodes and build up layer by layer to create thin films.[30] The scanning electron microscopy (SEM) micrographs of the HEH NPs can be observed in Figure 2, showing both the films and NPs that formed. Figures 2A and 2D show the film and NPs that formed on the electrodes under low current conditions. At a current density of 10 mA/cm^2, a uniform thin film formed on the electrode with no NPs found in the electrolyte. The NPs that formed the thin film were attached together as a result of the slower reaction kinetics caused by the low current conditions. The slower kinetics formed a network of NPs which creates the uniform thin film. Figures 2B and 2E show the film and NPs that formed

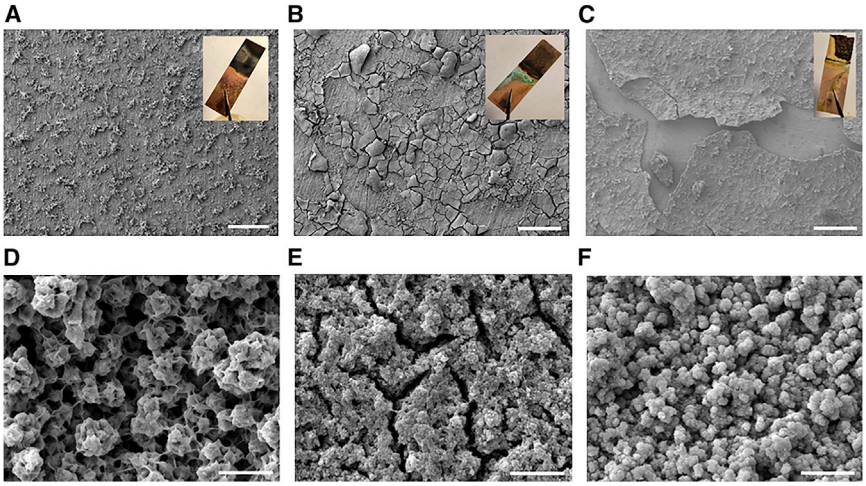

Figure 2. Morphology of the HEH at various current densities

(A) HEH film formed at 10 mA/cm^2.

(B) HEH film formed at 116 mA/cm^2.

(C) HEH film formed at 232 mA/cm^2 (scale bars for A–C represents 200 μm).

(D) HEH NPs formed at 10 mA/cm^2.

(E) HEH NPs formed at 116 mA/cm^2.

(F) HEH NPs formed at 232 mA/cm^2 (scale bars for D–F represents 1 μm).

at 116 mA/cm^2. The film that formed was no longer uniform, but consisted of large sections of NPs loosely bound to the electrode surface. The kinetics at this current density do not allow for uniform film formation. The non-uniformity of the film is shown in areas where the copper substrate can be seen between regions. Most NPs remained suspended in the electrolyte after synthesis. The shape of these NPs was changed from the low current conditions and no longer formed a network of connected particles. The NPs that formed were individual NPs with a polygonal shape. The NPs at this current density have a similar morphology to the NPs synthesized at 60 mA/cm^2, which are studied in detail in future sections. Figures 2C and 2F show the film and NPs that formed at 232 mA/cm^2. Under these current densities, the kinetics do not allow for a thin film to form. The NPs form quickly and are loosely attached to the electrode with most NPs found suspended in the electrolyte. The kinetics under high current densities makes it hard for large particles to agglomerate as they quickly form near the electrode and are released back into the electrolyte. As the current density is increased, the ability to make a thin film material is decreased and the morphology of the NPs changes as a result of the kinetics of the synthesis process.

Phase stability of HEH NPs

The stability of the HEH NPs comes not only from the higher entropy of having multiple elements, but also from the kinetics of the synthesis. The fast kinetics during synthesis do not allow for segregation of the various elements within the NPs. This is similar to the carbo-thermal shock synthesis method, in which the material is heated rapidly using an electric current and then cooled at a high rate (10^5 K/s).[34] The carbo-thermal shock method is able to produce compositions that range from unary systems up to octonary of high entropy alloy NPs. When the synthesis process is used at low currents and voltages, phase stability can be affected when using a low elemental count.[31] The phase stability can be overcome at low current and voltage conditions by including a greater number of elements.[2] Alternatively, by using a synthesis technique with fast kinetics, phase stability can be overcome and allows for the

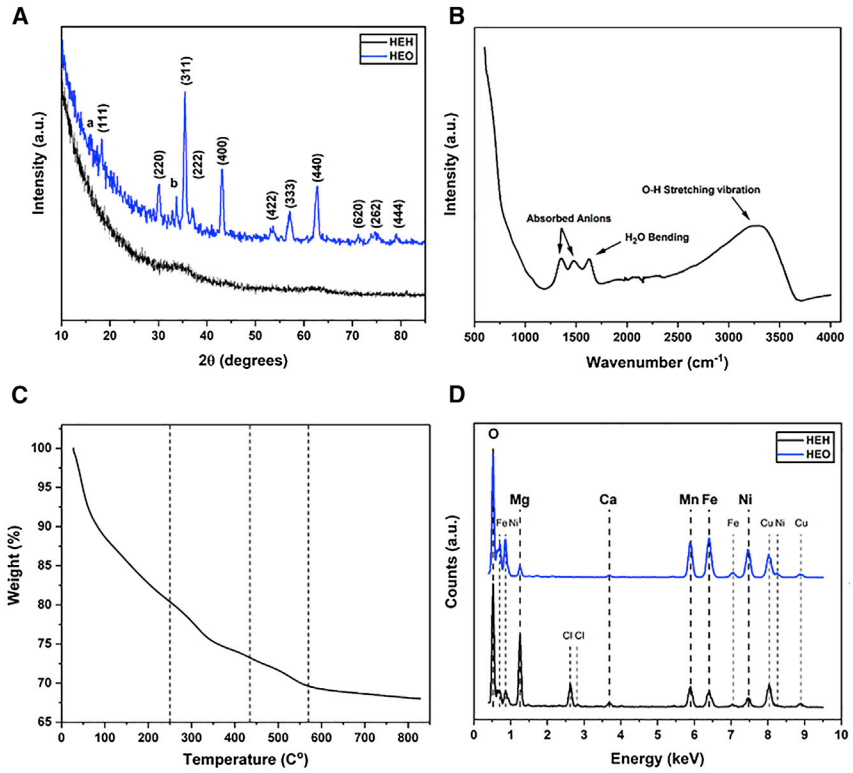

Figure 3. Structural characterization of HEH and HEO

(A) XRD of HEH and calcined HEO NPs.

(B) FTIR of HEH NPs.

(C) TGA of HEH NPs.

(D) EDS spectrum of HEH and calcined HEO NPs at 800°C for 3 h in air. (All particles synthesized at 60 mA/cm^2).

synthesis of multiple phase stable compositions.[34] This makes the synthesis process more robust; a number of compositions can be synthesized by changing the electrolyte composition.

Crystal structure characterization of HEH and HEO NPs

A quinary composition consisting of Fe, Mn, Ni, Ca, and Mg was synthesized using the ECS process. X-ray diffraction (XRD) was performed on the HEH to study the structure of the NPs. XRD spectra for both samples can be referred to in Figure 3A. The HEH displayed peaks similar to those found in other HEHs with two broad peaks found at 2θ of 34.8 and 62.7°.[8,10,11,35] Common layered hydroxides have basal planes assigned to (006) and (003) at low 2θ angles, which is used to measure interlayer spacing in a layered double hydroxide.[8,10,11,35] As the distance between the basal planes increases, the intensity of these peaks tends to decrease.[8,11] The synthesized HEH show no discernable peaks in this region suggesting an amorphous material.[7,8,36]

In addition to the HEH NPs, a simple calcination of the HEH allows for the formation of HEO NPs and films. The HEH was calcined at 800°C for 3 h in air. The XRD spectra seen in Figure 3A confirm that the HEH's structure has changed into a cubic spinel crystal structure upon calcination. The calcined powder had 12 affiliated peaks (111), (220), (310), (311), (222), (400), (422), (333), (440), (620), (262), and (444) crystal lattice planes, corresponding with the cubic spinel metal oxide crystal structure.[1,37]

The lattice constant for the calcined sample was measured to be 8.4005 Å. Two additional peaks (labeled a and b) were also present but are not characteristic peaks of the standard cubic spinel crystal structure. The occurrence of an extra XRD peak in the case of HEO NPs is possibly due to the lattice distortion established by charge density accumulation.[38]

In addition to the synthesis at 60 mA/cm^2, the NPs were also synthesized at 116 and 387 mA/cm^2 to determine any structural changes that might occur owing to the higher current densities. As seen in Figure S3A for the HEH, the same broad peaks found at 60 mA/cm^2 were also found at 116 and 387 mA/cm^2. Similarly, the calcined HEO NPs in Figure S3B all showed the same cubic spinel crystal structure. It was found that at higher current densities that additional peaks not found in the cubic spinel crystal structure (labeled a and b) were reduced and eliminated entirely at 387 mA/cm^2.

The Fourier transform infrared (FTIR) spectrum shown in Figure 3B shows a broad and strong band with a peak at 3310 cm^{-1}. The peak is assigned to the O-H stretching vibration of the hydroxyl group.[6,8,39] The peak at 1628 cm^{-1} is assigned to the bending of the water molecules.[6] The peaks from 1250 to 1500 cm^{-1} are the result of absorbed Cl anions.[12] Figure S4 shows a similar FTIR spectrum for the synthesis at 387 mA/cm^2.

A thermogravimetric analysis (TGA) was performed on the HEH up to 800°C to study the thermal decomposition of the HEH. The TGA spectrum shown in Figure 3C has four temperature regions. In the temperature range from 25°C to 250°C, the surface weakly absorbed water molecules and the interlayer water is removed (dehydration process).[40] The second temperature range occurs between 250°C and 435°C, and the mass loss is attributed to the thermal decomposition of the hydroxide to the respective oxide (dehydroxylation process).[41] The Cl anions was lost in the third temperature range between 435°C and 570°C.[13] The fourth range starts at 570°C and continues to 800°C, where the mass loss stabilizes and the HEO forms. The total mass loss over the temperature range was 32%.

The energy dispersive X-ray spectroscopy (EDS) spectrum in Figure 3D highlights the major and minor peaks for all six elements for both the HEH and calcined HEO NPs. As expected, the spectrum shows the removal of Cl anions from the HEH as the sample was calcinated; Cl anions break down at higher temperatures.

To analyze the bonding, the HEH NPs were studied using Raman spectroscopy. The acquired Raman spectrum can be observed in Figure S5. The two main Raman peaks associated with the HEH NPs are a broad single band located at 383.13 cm^{-1} with a full width at half maximum (FWHM) of 146.09 cm^{-1} and a broad single band located at 801.76 cm^{-1} with an FWHM of 154.34 cm^{-1}. The peak located at 383.13 cm^{-1} is attributed to translation parallel to the layers and M−O stretching vibrations from the various metal ions.[6,42] The peak located at 801.76 cm^{-1} is attributed to librations.[42] A smaller third broad band is located at 1045.21 cm^{-1} with an FWHM of 33.65 cm^{-1}. Cation disordering and overall disorder in the structure, which is a characteristic of high entropy materials, has been shown to cause peak broadening in the Raman spectrum.[43,44] A smaller NP size has also shown to contribute to peak broadening.[45] It has been reported that other hydroxides, such as $Ba(OH)_2$ and $Sr(OH)_2$, have Raman peaks in the 500–900 cm^{-2} region.[46] The broad peaks are a result of multiple contributions from the various elements in the HEH.

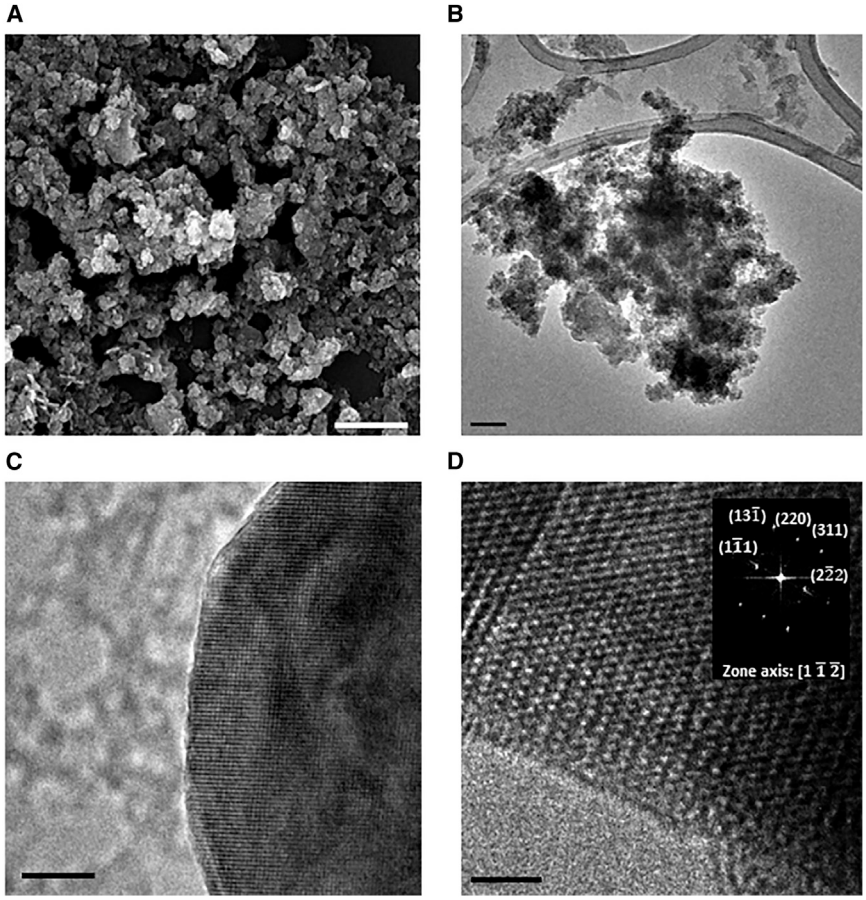

Figure 4. Microscopy of HEH and HEO NPs at 60 mA/cm^2

(A) SEM micrograph of the HEH NPs (scale bar, 500 nm).

(B) High resolution TEM of HEH NPs (scale bar, 50 nm).

(C) High resolution TEM of calcined HEO at 800°C for 3 h in air (scale bar, 5 nm).

(D) Atomic scale high resolution TEM of calcined HEO NPs at 800°C for 3 h in air (scale bar, 2 nm) with inset of an FFT analysis indicating the selected planes corresponding to the spinel cubic metal oxide crystal structure.

Microscopy of HEH and HEO NPs

The micrographs of the HEH and HEO can be observed below in Figure 4. The SEM micrograph of the HEH NPs can be observed in Figure 4A. The NPs had an average size of 37.53 $\pm$ 3.72 nm with particles ranging from 16 to 88 nm. The HR-TEM micrographs of the amorphous HEH NPs can be observed in Figure 4B, while those of the calcinated HEO NPs can be observed in Figure 4C. The atomic resolution crystal structure of calcined HEO NPs and its corresponding fast Fourier transform (FFT) analysis along the [1$\bar{1}$2] zone axis is shown in Figure 4D. The FFT consists of several diffraction spots attributed to the (1$\bar{1}$1), (220), (13$\bar{1}$), (311), and (222) planes corresponding with *d*-spacings of 4.96 Å, 3.1 Å, 2.58 Å, 2.57 Å, and 2.46 Å, respectively, which confirms the cubic spinel metal oxide crystal structure.[37] The HR-TEM analysis of the crystal structure of calcined HEO NPs is in line with those analyzed from the XRD spectrum.

Elemental composition of HEH NPs

To determine the synthesis processes' flexibility, a binary metal hydroxide and oxide along with a quinary HEH and HEO were synthesized at 60 mA/cm^2. EDS was

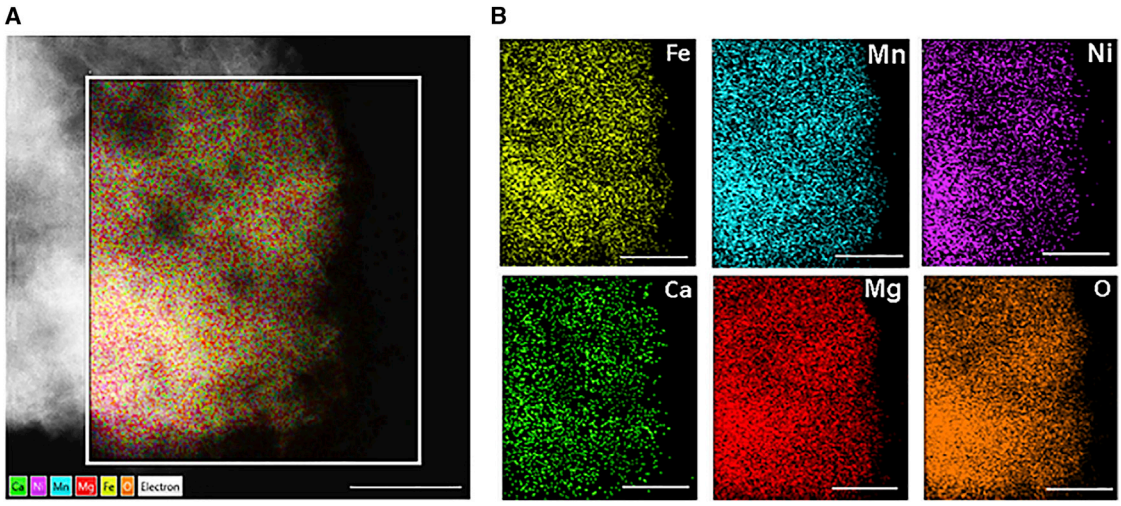

Figure 5. The chemical composition of the HEH NPs synthesized at 60 mA/cm^2

(A) EDS elemental mapping of HEH NPs.

(B) Compositional maps for individual elements of Fe, Mn, Ni, Ca, Mg, and O in HEH (scale bars, 100 nm).

performed on the binary metal hydroxide and quinary HEH NPs to determine their elemental composition. Figure 5 shows the elemental compositional characterization of the quinary HEH NPs. Figure 5A shows the elemental mapping within the quinary $[Ni_aMn_bFe_cCa_dMg_e]_xOH_y$ HEH NPs. The respective individual elemental distributions can be observed in Figure 5B. The atomic weight percentage for the quinary HEH NPs by elements are O (50.00%), Fe (6.4%), Mn (8.0%), Ni (3.6), Ca (1.5%), and Mg (30.5%). The quinary HEH NPs form in a high entropy state during the synthesis process without any additional steps as confirmed by EDS measurements observed in Figure 5B.

Magnesium in the HEH had the highest concentration owing to the kinetic effects it had during the dynamic synthesis process. The faster kinetics is largely due to the smaller mass of Mg compared with the other cations in solution. The force the ions feel during synthesis is based on the magnitude of the electric field and the charge of each ion, which is derived from Coulomb's Law.[30] Mg has faster kinetics during synthesis, which causes it to move at a higher rate. The synthesis process relies on the movement of particles in an electric field, which is affected by ion sizes, masses, and charges. These parameters affect the kinetics, which affects the final composition of the synthesized HEH NPs. If near equimolar concentration within the final metal oxide structure is desired, the precursor concentrations can be adjusted in the electrolyte in order to account for variations in elemental properties and synthesis kinetics.[47] An electron energy loss spectroscopy (EELS) elemental analysis was performed on the HEH NPs to ensure the mixing of elements at the subnanometer scale. Figure S6 highlights the EELS spectra in the O, Mn, and Fe regions and shows the high level of mixing in the HEH NPs.

Figure S7 shows the elemental mapping of the binary metal hydroxide NPs. The elements in the binary metal hydroxide were Fe and Mn. The EDS elemental mapping of the binary metal hydroxide can be seen in Figure S7A. The respective individual elemental distributions can be observed in Figure S7B. The atomic weight percentage for the binary metal hydroxide by elements are Fe (29.1%), Mn (20.9%), and O (50.0%). Figure S7C shows the EDS spectrum of the binary metal hydroxide NP with Fe and Mn metal cations.

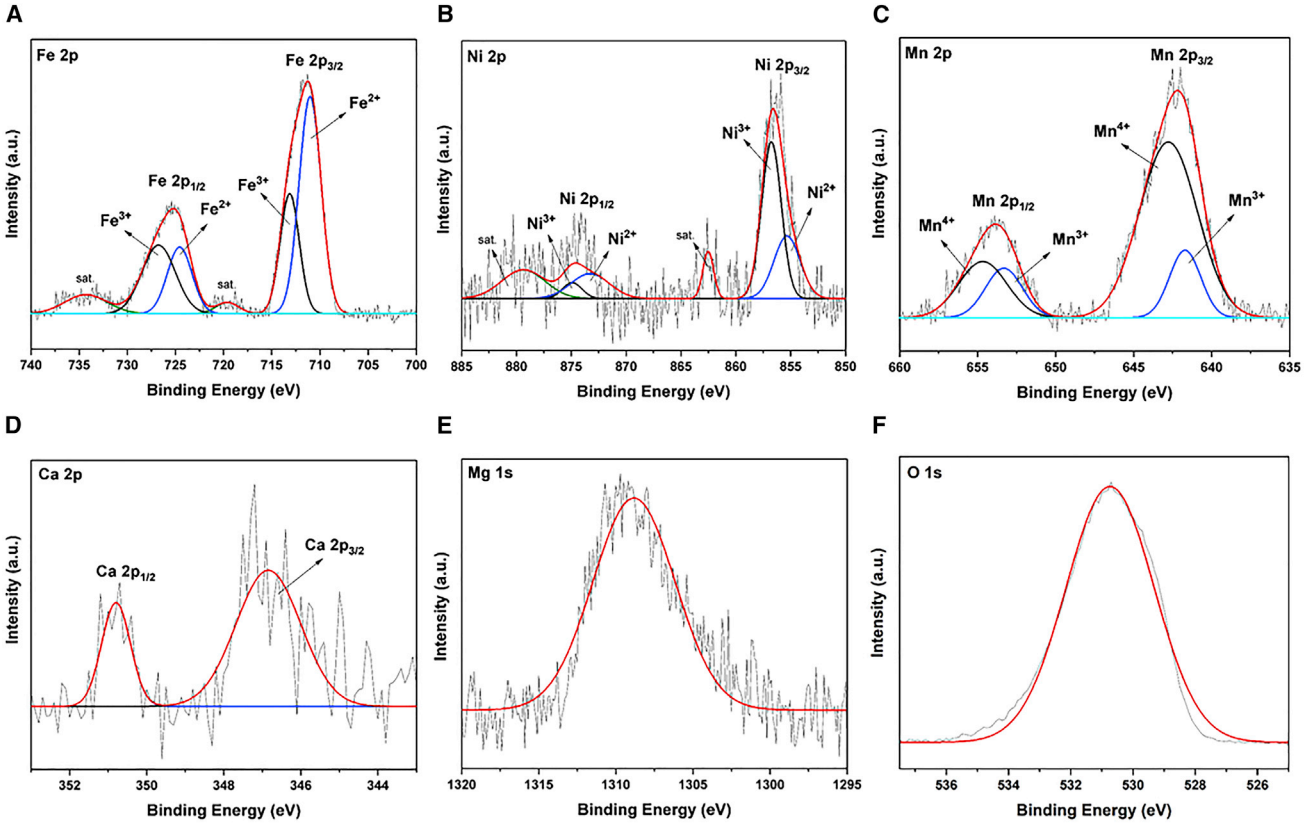

Figure 6. High-resolution XPS spectra of HEH at 60 mA/cm^2

(A) Fe 2p spectra of HEH.
(B) Ni 2p spectra of HEH.
(C) Mn 2p spectra of HEH.
(D) Ca 2p spectra of HEH.
(E) Mg 1s spectra of HEH.
(F) O 1s spectra of HEH.

Figure S9 highlights the EDS of a standard specimen of MnO (Sigma-Aldrich 377201) and MnO_2 (Sigma Aldrich 243442). The standard specimen should contain an oxygen content of 66.67 atomic percent for MnO_2 and 50 atomic percent for MnO. There is a possibility for a maximum of 8.04% error with the quantification of oxygen based on the calibration data on MnO and MnO_2. To further improve compositional accuracy, induced coupled plasma spectroscopy can be performed on the HEH NPs.

Chemical oxidation analysis of HEH NPs

X-ray photoelectron spectroscopy (XPS) was used to characterize the elemental states in the HEH NPs. Fine scans of various elements can be seen in Figures 6A–6F. Figure 6A shows the high-resolution spectra for Fe 2p and is fitted with two doublet peaks along with satellite peaks. The first peak located at 711.26 eV is assigned to $2p_{3/2}$ and the peak at 725.23 eV is assigned to $2p_{1/2}$ with an energy splitting of 13.97 eV. The $2p_{3/2}$ and $2p_{1/2}$ peaks can be deconvoluted into peaks representing the Fe^{2+} and Fe^{3+} oxidation states with the peaks at 711.00 eV (Fe $2p_{3/2}$) and 724.60 eV (Fe $2p_{1/2}$) being attributed to Fe^{2+} and the peaks at 713.10 eV (Fe $2p_{3/2}$) and 726.70 eV (Fe $2p_{1/2}$) being attributed to Fe^{3+}.[16,48] In Figure 6B, the high-resolution XPS spectra of Ni is shown, representing the 2p core energy states. This includes two main peaks located at 856.6 and 874.59 eV, which represent the

$2p_{3/2}$ and $2p_{1/2}$ spin orbits and two satellite peaks. The peaks have an energy splitting of 17.99 eV. The satellite peaks represent the presence of mixed valence oxidation states for Ni. The deconvoluted peaks located at 855.30 eV (Ni $2p_{3/2}$) and 873.30 eV (Ni $2p_{1/2}$) are related to Ni^{2+}, while the peaks at 856.80 eV (Ni $2p_{3/2}$) and 874.90 eV (Ni $2p_{1/2}$) are related to Ni^{3+}.[48] Figure 6C shows the high-resolution spectra of Mn 2p, which forms a doublet of two peaks. The first peak located at 642.18 eV is assigned to Mn $2p_{3/2}$ and the second peak located at 653.84 eV is assigned to Mn $2p_{1/2}$ and has an energy splitting of 11.66 eV, which is similar to previous reports on Mn_3O_4.[49] To determine the oxidation states present in the HEH, the peaks were deconvoluted. The deconvoluted peaks located at 641.70 eV (Mn $2p_{3/2}$) and 653.32 eV (Mn $2p_{1/2}$) are associated with Mn^{3+}, while the peaks at 642.78 eV (Mn $2p_{3/2}$) and 654.66 eV (Mn $2p_{1/2}$) are associated with Mn^{4+}.[50] Figure 6D shows the high-resolution spectra for Ca 2p. Two main peaks are located at 346.83 eV (Ca $2p_{3/2}$) and 350.80 eV (Ca $2p_{1/2}$). Figure 6E shows the high-resolution spectra for Mg 1s with the main peak located at 1308.8 eV showing the incorporation of Mg into the structure. The high-resolution spectra of the O 1s peak is shown in Figure 6F. It shows an intense peak at 530.74 eV, which is characteristic of OH^- peaks in metal hydroxides.[51] The peaks for all elements have been shifted slightly from their characteristic metal peaks, which is attributed to the metal-oxygen bonding in the lattice. A shift to higher energies is common with this type of bonding in high entropy materials.[52,53] The XPS survey spectrum can be seen in Figure S8 and highlights all the chemical elements in the HEH.

DISCUSSION

This study was successful in synthesizing HEH and HEO NPs through ECS techniques in an aqueous environment using the hydrogen evolution reaction. Microscopic investigations show that, by taking advantage of the hydrogen evolution reaction, multi-elemental compositions can be formed. It showed that the HEH NPs can be processed into an HEO upon calcination. The FTIR, TGA, and XPS studies confirmed the presence of the HEH and HEO NPs. The EDS of the HEH NPs was able to confirm the chemical mixing of elements down to the atomic scale. The reported ECS technique can be used for synthesizing multi-element compositions with substrate-free NPs. The process is compatible with a vast choice of precursors, which can be used in the future to tune the composition of both the HEH and HEO NPs.

EXPERIMENTAL PROCEDURES

Resource availability

Lead contact

Further information and requests for resources should be directed to and will be fulfilled by the lead contact, Reza Shahbazian-Yassar (rsyassar@uic.edu).

Materials availability

All salts were analytical grade and used as received. $FeCl_3$ and $CaCl_2$ were purchased from Sigma Aldrich, $NiCl_2$ was purchased from Millipore Sigma, $MnCl_2 \cdot 4H_2O$ was purchased from Fischer Scientific. $MgCl_2$ was purchased from Alfa Aesar.

Data and code availability

All original data generated and analyzed during this study are included in this article and the supplemental information or are available upon request from the lead contact. No original code was generated for this report.

Materials

The binary metal hydroxide and quinary HEH NPs were synthesized using an electrochemical deposition process. The binary and quinary particles were made from $MnCl_2 \cdot 4H_2O$, $NiCl_2$, $FeCl_3$, $CaCl_2$, & $MgCl_2$. The salts were mixed at a concentration of 0.1 M in 25 mL of deionized (DI) water. The electrolyte solution was then stirred for 1 h to make sure the salts were well dissolved in solution.

Synthesis

The HEH NP synthesis was performed at room temperature using an aqueous-based ECS process. The electrolyte is prepared by mixing metal salt precursors and DI water. The ECS process was carried out in a two electrode system consisting of a copper cathode and a graphite anode. The cathode was a rectangular piece of copper foil with a submersed area of 22.5 × 11.5 mm, while the anode was a cylindrical piece of graphite with a submersed area of 22.5 (L) × 3 mm (D). The two electrodes were spaced roughly 10 mm apart. A Keithley 2400 Source Meter was used to apply a constant current density of 10, 60, 116, 232, and 386 mA/cm^2 to the electrolyte solution. The current was supplied for several minutes until a noticeable amount of material was formed in the solution.

Characterization

The synthesized NPs that formed were collected, centrifuged, cleaned in DI water, and dried into a powder. A microscopy sample preparation was done by dispersing the NPs in methanol and drop-casting the solution onto a 300-mesh carbon-coated copper grid. Morphological and high-resolution transmission electron microscopy images were collected by a JEOL ARM200CF. Energy dispersive spectroscopy (EDS) was performed using an aberration corrected JEOL ARM200CF with a cold field emission gun operated at 200 kV, equipped with an Oxford X-max 100TLE windowless X-ray detector. Scanning electron microscope (SEM) measurements were performed on a 30-kV JEOL JSM-IT500HR. Raman spectroscopy was performed on a Renishaw inVia Reflex with a green 532-nm laser with a 10 s exposure. XPS was performed using a ThermoFisher Scientific ESCALAB 250Xi to detect the chemical states of the HEH nanomaterials. Carbon tape was used to secure the sample. The spectra were calibrated with adventitious carbon at 284.8 eV. XRD was performed on a Bruker D8 with a 2θ range of 10° to 85°. The resolution was 0.02° with time steps of 1 s. FTIR was performed on a Thermo Nicolet Nexus 870 spectrometer in attenuated total reflection mode. The range was 600–4000 cm^{-1} with an average of 64 scans at a 4 cm^{-1} resolution. Results were converted to percent of transmittance using OMNIC spectra software. A TGA was performed on a Texas Instruments Q5000 with a heating rate of 10°C/min.

SUPPLEMENTAL INFORMATION

Supplemental information can be found online at https://doi.org/10.1016/j.xcrp.2022.100847.

ACKNOWLEDGMENTS

The authors acknowledge financial support from National Science Foundation DMR-1809439. In addition, we thank the fellowship granted to J.M.G. (FAPESP 2020/06176-7).

AUTHOR CONTRIBUTIONS

T.G.R. developed the concept, designed the experiment, analyzed the experimental data, and performed the XRD characterization. A.H.P. performed and

analyzed the STEM microscopy and EDS spectroscopy. M.G.R. performed XPS, TGA, and FTIR spectroscopy. L.V.S. performed Raman spectroscopy. M.TS. performed the SEM microscopy. J.M.G. analyzed TGA. T.S. provided instrument support. J.M.G. and R.S.Y. directed the project. T.G.R, J.M.G., and R.S.Y wrote the manuscript. All of the authors discussed the results and commented on the manuscript.

DECLARATION OF INTERESTS

The authors declare no conflict of interest.

Received: September 8, 2021
Revised: February 22, 2022
Accepted: March 17, 2022
Published: April 8, 2022

REFERENCES

1. Dąbrowa, J., Stygar, M., Mikuła, A., Knapik, A., Mroczka, K., Tejchman, W., Marek, D., and Martin, M. (2018). Synthesis and microstructure of the (Co,Cr,Fe,Mn,Ni)3O4 high entropy oxide characterized by spinel structure. Mater. Lett. *216*, 32–36. https://doi.org/10.1016/j.matlet.2017.12.148.

2. Aliyu, A., and Srivastava, C. (2019). Microstructure-corrosion property correlation in electrodeposited AlCrFeCoNiCu high entropy alloys-graphene oxide composite coatings. Thin Solid Films *686*, 137434. https://doi.org/10.1016/j.tsf.2019.137434.

3. Bérardan, D., Franger, S., Meena, A.K., and Dragoe, N. (2016). Room temperature lithium superionic conductivity in high entropy oxides. J. Mater. Chem. A *4*, 9536–9541. https://doi.org/10.1039/c6ta03249d.

4. Sarkar, A., Velasco, L., Wang, D., Wang, Q., Talasila, G., de Biasi, L., Kubel, C., Brezesinski, T., Bhattacharya, S.S., Hahn, H., et al. (2018). High entropy oxides for reversible energy storage. Nat. Commun. *9*. https://doi.org/10.1038/s41467-018-05774-5.

5. Yao, C.Z., Zhang, P., Liu, M., Li, G.R., Ye, J.Q., Liu, P., et al. (2008). Electrochemical preparation and magnetic study of Bi-Fe-Co-Ni-Mn high entropy alloy. Electrochim. Acta *53*, 8359–8365. https://doi.org/10.1016/j.electacta.2008.06.036.

6. Zhang, Z., and Li, H. (2021). Promoting the uptake of chloride ions by ZnCo-Cl layered double hydroxide electrodes for enhanced capacitive deionization. Environ. Sci. Nano *8*, 1886–1895. https://doi.org/10.1039/d1en00350j.

7. Pan, J., Bao, Y., Wang, H., Lyu, F., Liu, L., Wang, C., Tang, X., Lu, J., and Li, Y.Y. (2021). Amorphous high-entropy hydroxides of tunable wide solar absorption for solar water evaporation. Part. Part. Syst. Char. *38*, 1–6. https://doi.org/10.1002/ppsc.202100094.

8. Gu, K., Zhu, X., Wang, D., Zhang, N., Huang, G., Li, W., Long, P., Tian, J., Zou, Y., Wang, Y., et al. (2021). Ultrathin defective high-entropy layered double hydroxides for electrochemical water oxidation. J. Energy Chem. *60*, 121–126. https://doi.org/10.1016/j.jechem.2020.12.029.

9. Wang, Q., and Ohare, D. (2012). Recent advances in the synthesis and application of layered double hydroxide (LDH) nanosheets. Chem. Rev. *112*, 4124–4155. https://doi.org/10.1021/cr200434v.

10. Duan, X., Evans, D.G., He, J., Kang, Y., Khan, A.I., Leroux, F., et al. (2006). In Layered Double Hydroxides, X. Duan and D.G. Evans, eds. (Springer). https://doi.org/10.1007/b100426.

11. Hunter, B.M., Hieringer, W., Winkler, J.R., Gray, H.B., and Müller, A.M. (2016). Effect of interlayer anions on [NiFe]-LDH nanosheet water oxidation activity. Energy Environ. Sci. *9*, 1734–1743. https://doi.org/10.1039/c6ee00377j.

12. Jayashree, R.S., and Vishnu Kamath, P. (1999). Factors governing the electrochemical synthesis of α-nickel (II) hydroxide. J. Appl. Electrochem. *29*, 449–454. https://doi.org/10.1023/A:1003493711239.

13. Mahjoubi, F.Z., Khalidi, A., Abdennouri, M., and Barka, N. (2017). Zn–Al layered double hydroxides intercalated with carbonate, nitrate, chloride and sulphate ions: synthesis, characterisation and dye removal properties. J. Taibah Univ. Sci. *11*, 90–100. https://doi.org/10.1016/j.jtusci.2015.10.007.

14. Bérardan, D., Franger, S., Dragoe, D., Meena, A.K., and Dragoe, N. (2016). Colossal dielectric constant in high entropy oxides. Phys. Status Solidi - Rapid Res. Lett. *10*, 328–333. https://doi.org/10.1002/pssr.201600043.

15. Kumar, N., Tiwary, C.S., and Biswas, K. (2018). Preparation of nanocrystalline high-entropy alloys via cryomilling of cast ingots. J. Mater. Sci. *53*, 13411–13423. https://doi.org/10.1007/s10853-018-2485-z.

16. Phakatkar, A.H., Saray, M.T., Rasul, G., Sorokina, L.V., Ritter, T., Shokuhfar, T., and Shahbazian-Yassar, R. (2021). Ultrafast Synthesis of High Entropy Oxide Nanoparticles by Flame Spray Pyrolysis. Langmuir *37*, 9059–9068. https://doi.org/10.1021/acs.langmuir.1c01105.

17. Yang, Y., Ghildiyal, P., and Zachariah, M.R. (2019). Thermal shock synthesis of metal nanoclusters within on-the-fly graphene particles. Langmuir *35*, 3413–3420. https://doi.org/10.1021/acs.langmuir.8b03532.

18. Singh, M.P., and Srivastava, C. (2015). Synthesis and electron microscopy of high entropy alloy nanoparticles. Mater. Lett. *160*, 419–422. https://doi.org/10.1016/j.matlet.2015.08.032.

19. Haché, M.J.R., Tam, J., Erb, U., and Zou, Y. (2022). Electrodeposited nanocrystalline medium-entropy alloys – an effective strategy of producing stronger and more stable nanomaterials. J. Alloys Compd. *899*, 163233. https://doi.org/10.1016/j.jallcom.2021.163233.

20. Kemény, D.M., Pálfi, N.M., and Fazakas, É. (2020). Examination of microstructure and corrosion properties of novel AlCoCrFeNi multicomponent alloy. Mater. Today Proc. *45*, 4250–4253. https://doi.org/10.1016/j.matpr.2020.12.285.

21. Popescu, A.M.J., Branzoi, F., Constantin, I., Anastasescu, M., Burada, M., Mitrică, D., Anasiei, I., Olaru, M.T., and Constantin, V. (2021). Electrodeposition, characterization, and corrosion behavior of CoCrFeMnNi high-entropy alloy thin films. Coatings *11*, 1367. https://doi.org/10.3390/coatings11111367.

22. Soare, V., Burada, M., Constantin, I., Mitricə, D., Bədiliță, V., Caragea, A., and Tarcolea, M. (2015). Electrochemical deposition and microstructural characterization of AlCrFeMnNi and AlCrCuFeMnNi high entropy alloy thin films. Appl. Surf. Sci. *358*, 533–539. https://doi.org/10.1016/j.apsusc.2015.07.142.

23. Zeng, Z., Zhang, W., Liu, Y., Lu, P., and Wei, J. (2017). Uniformly electrodeposited α-MnO2 film on super-aligned electrospun carbon nanofibers for a bifunctional catalyst design in oxygen reduction reaction. Electrochim. Acta *256*, 232–240. https://doi.org/10.1016/j.electacta.2017.10.057.

24. Boccaccini, A.R., Cho, J., Roether, J.A., Thomas, B.J.C., Jane Minay, E., and Shaffer, M.S.P. (2006). Electrophoretic deposition of carbon nanotubes. Carbon N. Y *44*, 3149–3160. https://doi.org/10.1016/j.carbon.2006.06.021.

25. Liu, Y., Zeng, Z., Sharma, R.K., Gbewonyo, S., Allado, K., Zhang, L., and Jianjun, W. (2019). A Bi-functional configuration for a metal-oxide

film supercapacitor. J. Power Sourc. *409*, 1–5. https://doi.org/10.1016/j.jpowsour.2018.10.084.

26. Kuhn, A.T., and Chan, C.Y. (1983). pH changes at near-electrode surfaces. J. Appl. Electrochem. *13*, 189–207. https://doi.org/10.1007/BF00612481.

27. Boyer, R.F. (1993). Modern Experimental Biochemistry, Second (The Benjamin/Cummings Publishing Company).

28. Williams, B., and Wilson, K. (1975). A Biologist's Guide to Principles and Techniques of Practical Biochemistry (Edward Arnold).

29. Plummer, D. (1987). An Introduction to Practical Biochemistry, Third (McGraw-Hill).

30. Sarkar, P., and Nicholson, P.S. (1996). Electrophoretic deposition (EPD): mechanisms, kinetics, and application to ceramics. J. Am. Ceram. Soc. *79*, 1987–2002. https://doi.org/10.1111/j.1151-2916.1996.tb08929.x.

31. Sun, Y., and Zangari, G. (2019). Phase separation in electrodeposited Ag-Pd alloy films from acidic nitrate bath. J. Electrochem. Soc. *166*, D339–D349. https://doi.org/10.1149/2.1231908jes.

32. Yoosefan, F., Ashrafi, A., and Monir Vaghefi, S.M. (2020). The feasibility of producing CoCrFeMnNi high entropy alloy coatings by electrochemical deposition method and its characterization. J. Metall. Mater. Eng. *31*, 109–120.

33. Zheng, M., Li, Y., Hu, J., Zhao, Y., and Yu, L. (2014). Preparation of high entropy alloy thin film fenicobimn by electroplating deposition method. Nucl. Instrum. Methods Phys. Res. Sect. B Beam Interact. Mater. Atoms *76*, 1–5.

34. Yao, Y., Huang, Z., Xie, P., Lacey, S.D., Jacob, R.J., Xie, H., Chen, F., Nie, A., Pu, T., and Hu, L. (2018). Carbothermal shock synthesis of high-entropy-alloy nanoparticles. Science *359*, 1489–1494. https://doi.org/10.1126/science.aan5412.

35. Vaysse, C., Guerlou-Demourgues, L., and Delmas, C. (2002). Thermal evolution of carbonate pillared layered hydroxides with (Ni, L) (L = Fe, Co) based slabs: grafting or nongrafting of carbonate anions? Inorg. Chem. *41*, 6905–6913. https://doi.org/10.1021/ic025542r.

36. Nethravathi, C., Viswanath, B., Sebastian, M., and Rajamathi, M. (2010). Exfoliation of α-hydroxides of nickel and cobalt in water. J. Colloid Interf. Sci. *345*, 109–115. https://doi.org/10.1016/j.jcis.2010.01.047.

37. Jain, A., Ong, S.P., Hautier, G., Chen, W., Richards, W.D., Dacek, S., Cholia, S., Gunter, D., Skinner, D., Ceder, G., et al. (2013). Commentary: the materials project: a materials genome approach to accelerating materials innovation. APL Mater. *1*. https://doi.org/10.1063/1.4812323.

38. Kalinowski, L., Goraus, J., and Slebarski, A. (2018). "DistorX" program for analysis of structural distortions affecting X-ray diffraction patterns. AIP Adv. *8*. https://doi.org/10.1063/1.5042654.

39. Ma, P., Zhang, S., Zhang, M., Gu, J., Zhang, L., Sun, Y., Ji, W., and Fu, Z. (2020). Hydroxylated high-entropy alloy as highly efficient catalyst for electrochemical oxygen evolution reaction. Sci. China Mater. *63*, 2613–2619. https://doi.org/10.1007/s40843-020-1461-2.

40. Wang, D., Xu, R., Wang, X., and Li, Y. (2006). NiO nanorings and their unexpected catalytic property for CO oxidation. Nanotechnology *17*, 979–983. https://doi.org/10.1088/0957-4484/17/4/023.

41. de Matos, C.S., Nóbrega, M.M., Temperini, M.L.A., and Constantino, V.R.L. (2019). Hybrid Ni–Al layered double hydroxide: characterization and in situ synchrotron XRD and vibrational spectroscopic studies under high-pressure. Appl. Clay Sci. *174*, 152–158. https://doi.org/10.1016/j.clay.2019.03.031.

42. Pascale, F., Tosoni, S., Zicovich-Wilson, C., Ugliengo, P., Orlando, R., and Dovesi, R. (2004). Vibrational spectrum of brucite, Mg(OH) 2: a periodic ab initio quantum mechanical calculation including OH anharmonicity. Chem. Phys. Lett. *396*, 308–315. https://doi.org/10.1016/j.cplett.2004.08.047.

43. Gouadec, G., and Colomban, P. (2007). Raman Spectroscopy of nanomaterials: how spectra relate to disorder, particle size and mechanical properties. Prog. Cryst. Growth Char. Mater. *53*, 1–56. https://doi.org/10.1016/j.pcrysgrow.2007.01.001.

44. D'Ippolito, V., Andreozzi, G.B., Bersani, D., and Lottici, P.P. (2015). Raman fingerprint of chromate, aluminate and ferrite spinels. J. Raman Spectrosc. *46*, 1255–1264. https://doi.org/10.1002/jrs.4764.

45. Arora, A.K., Rajalakshmi, M., Ravindran, T.R., and Sivasubramanian, V. (2007). Raman spectroscopy of optical phonon confinement in nanostructured materials. J. Raman Spectrosc. *38*, 604–617. https://doi.org/10.1002/jrs.1684.

46. Lutz, H.D., Eckers, W., Schneider, G., and Haeuseler, H. (1981). Raman and infrared spectra of barium and strontium hydroxides and hydroxide hydrates. Spectrochim. Acta Part A Mol. Spectrosc. *37*, 561–567. https://doi.org/10.1016/0584-8539(81)80048-7.

47. Yang, Y., Song, B., Ke, X., Xu, F., Bozhilov, K.N., Hu, L., Shahbazian-Yassar, R., and Zachariah, M.R. (2020). Aerosol synthesis of high entropy alloy nanoparticles. Langmuir *36*, 1985–1992. https://doi.org/10.1021/acs.langmuir.9b03392.

48. Wang, D., Liu, Z., Du, S., Zhang, Y., Li, H., Xiao, Z., Wei, C., Chen, R., Wang, Y., and Zou, Y. (2019). Low-temperature synthesis of small-sized high-entropy oxides for water oxidation. J. Mater. Chem. A *7*, 24211–24216. https://doi.org/10.1039/c9ta08740k.

49. Tholkappiyan, R., Naveen, A.N., Vishista, K., and Hamed, F. (2018). Investigation on the electrochemical performance of hausmannite Mn 3 O 4 nanoparticles by ultrasonic irradiation assisted co-precipitation method for supercapacitor electrodes. J. Taibah Univ. Sci. *12*, 669–677. https://doi.org/10.1080/16583655.2018.1497440.

50. Ramirez, A., Hillenbrand, P., Stellmach, D., May, M.M., Bogdanoff, P., and Fiechter, S. (2014). Evaluation of MnOx, Mn2O3, and Mn3O4 electrodeposited films for the oxygen evolution reaction of water. J. Phys. Chem. *118*, 14073–14081. https://doi.org/10.1021/jp500939d.

51. Dupin, J.C., Gonbeau, D., Vinatier, P., and Levasseur, A. (2000). Systematic XPS studies of metal oxides, hydroxides and peroxides. Phys. Chem. Chem. Phys. *2*, 1319–1324. https://doi.org/10.1039/a908800h.

52. Mcintyre, N.S., and Cook, M.G. (1975). X-ray photoelectron studies on some oxides and hydroxides of cobalt, nickel, and copper. Anal. Chem. *47*, 2208–2213. https://doi.org/10.1021/ac60363a034.

53. Xu, X., Guo, Y., Bloom, B.P., Wei, J., Li, H., Li, H., Du, Y., Zeng, Z., Li, L., and Waldecl, L.D. (2020). Elemental core level shift in high entropy alloy nanoparticles via X-ray photoelectron spectroscopy analysis and first-principles calculation. ACS Nano *14*, 17704–17712. https://doi.org/10.1021/acsnano.0c09470.